



HAL
open science

Arenaviridae NP-exonuclease inhibition by bisphosphonate

Thi Hong van Nguyen, Elsie Yekwa, Barbara Selisko, Bruno Canard, Karine Alvarez, Francois Ferron

► **To cite this version:**

Thi Hong van Nguyen, Elsie Yekwa, Barbara Selisko, Bruno Canard, Karine Alvarez, et al.. Arenaviridae NP-exonuclease inhibition by bisphosphonate. *IUCrJ*, 2022, 9 (4), 10.1107/S2052252522005061 . hal-03663359

HAL Id: hal-03663359

<https://amu.hal.science/hal-03663359>

Submitted on 10 May 2022

HAL is a multi-disciplinary open access archive for the deposit and dissemination of scientific research documents, whether they are published or not. The documents may come from teaching and research institutions in France or abroad, or from public or private research centers.

L'archive ouverte pluridisciplinaire **HAL**, est destinée au dépôt et à la diffusion de documents scientifiques de niveau recherche, publiés ou non, émanant des établissements d'enseignement et de recherche français ou étrangers, des laboratoires publics ou privés.



Distributed under a Creative Commons Attribution 4.0 International License

***Arenaviridae* NP-exonuclease inhibition by bisphosphonate**

**Thi Hong Van Nguyen^{1°}, Elsie Yekwa^{1°}, Barbara Selisko¹, Bruno Canard^{1,2},
Karine Alvarez¹ and François Ferron^{1,2*}**

¹ *Aix-Marseille Université and Laboratoire Architecture et Fonction des
Macromolécules Biologiques (AFMB), CNRS – UMR-7257, 13288 Marseille, France.*

² *European Virus Bioinformatics Center, Leutrargraben 1, 07743 Jena, Germany.*

[°]*The authors equally contributed to this work*

**Corresponding author : francois.ferron@univ-amu.fr*

Synopsis - Virtual screening, molecular docking and molecular characterization of *Arenaviridae* NP exonuclease inhibitor complex: Insight into structure-based drug design

Abstract

Abstract - Arenaviruses are emerging enveloped negative-sense RNA viruses which cause neurological and hemorrhagic diseases in humans. Currently there is no FDA approved vaccine or therapeutic agent except ribavirin which must be administered early during infection for optimum efficacy. A hallmark for arenavirus infection is a rapid and efficient immune-suppression mediated by the exonuclease domain encoded by the nucleoprotein. This exonuclease is therefore an attractive target for the design of novel antiviral drugs since exonuclease inhibitors might not only have a direct effect on the enzyme but could also boost viral clearance through stimulation of the innate immune system of the host cell. Here we have used an *in silico* screening and an enzymatic assay to identify a novel, specific but weak inhibitor of the arenavirus exonuclease with IC₅₀ values of 65.9 μM and 68.6 μM for Mopeia virus and Lymphocytic choriomeningitis virus, respectively. We further characterized this finding with crystallographic and docking approaches. This study serves as a proof of concept and may have assigned a new therapeutic purpose for the bisphosphonate family and therefore paves the way for the development of inhibitors against *Arenaviridae*.-

Keywords: - *Arenaviridae* ; exonuclease ; LCMV ; MOPV ; LASV ; Alendronate, compounds optimization; metal chelation.

1. Introduction

The genus *Mammarenavirus* belongs to the *Arenaviridae*, a family of neglected enveloped negative-sense RNA viruses associated with neurological and hemorrhagic diseases in humans. In South America, Machupo (MAV), Guanarito, Junin, Sabia, and Chapare viruses are responsible for hemorrhagic fever (Bowen et al., 1997) while in Africa Lujo virus (Briese *et al.*, 2009) and Lassa virus (LASV) constitute a major public health concern (Mofolorunsho, 2016; Peterson *et al.*, 2014; Yun & Walker, 2012). LASV is by far the biggest public health concern as its geographical distribution overlaps with the one of Ebola virus and other hemorrhagic viruses for which the clinical symptoms are very similar. LASV accounts annually for an estimated number of 300,000 to 500,000 infections leading to permanent and severe hearing loss, and death in the most severe cases (1% of the total infection number) (Günther and Lenz, 2004; Yun et al., 2015). The 2016 outbreak case fatality rate amongst patients has been determined at 37.9% with a spreading scenario (Nigeria, Benin, Togo, Liberia, imported cases in Germany and Sweden (WHO) . The most recent outbreak of 2019 lasted two months in Nigeria with a fatality rate amongst confirmed cases of 14 % (WHO.). There is currently no FDA-licensed vaccine nor therapeutic agent to protect against LASV infection except for ribavirin if administered early in the infection.

Mammarenaviruses have a bi-segmented genome composed of the L (large; ~ 7.3 kb) and S (small; ~ 3.5 kb) segments (Buchmeier *et al.*, 2007). Both segments encode two proteins. The L segment encodes protein L, which is the main actor of transcription and replication through an endonuclease domain (Morin *et al.*, 2010) and the RNA-dependent RNA polymerase (RdRp) domain (Ferron *et al.*, 2017). The second protein of the L segment is the matrix RING-finger protein Z. The S segment encodes the precursor of mature virion glycoprotein GP-C that will give after post-translational cleavage GP-1 and GP-2, and the nucleoprotein (NP). NP forms a polymer protecting the genomic (and anti-genomic) RNA (RNA_v) and is involved in innate immunity suppression (Hastie et al., 2011a; Jiang et al., 2013; Qi et al., 2010). L and NP together with RNA_v form an active ribonucleic complex for replication and transcription, that will remain in the cytoplasm (Pinschewer et al., 2003). One remarkable characteristic of arenavirus infection is the persistence of infection (Rawls et al., 1981). This is partly due to the ability of arenaviruses to control very efficiently the innate immune response of the infected host. NP and Z are directly involved in the regulation of type I interferon (IFN- α and IFN- β), and sequestration of interferon-stimulated genes (ISGs) (Meyer and Ly, 2016; Xing et al., 2015). NP possesses an exonuclease domain that is involved in suppressing double-stranded (ds) RNAs. These latter are markers of viral infection which triggers the host innate immunity response. Recently, the role of the exonuclease domain was proposed to be extended to replication as well (Huang et al., 2015;

Yekwa et al., 2019), promoting NP as a corner stone protein of arenavirus infection. Due to its role in innate immunity suppression and potentially in replication NP exonuclease (NP-exo) is an attractive target for the development of antiviral molecules.

The NP-exo structures of LCMV, LASV, and MOPV were previously characterized in the presence of divalent ions (Mg^{2+} or Mn^{2+}) (Hastie, Kimberlin et al., 2011; Jiang et al., 2013; Yekwa et al., 2017). The general mechanism for RNA hydrolysis follows a two metal ion mechanism (TMIC) described by Steitz and Steitz (Steitz and Steitz, 1993). It involves two metal ions positioned in the conserved catalytic pocket defined by residues D390, E392, D467, D534 (labeling of Mopeia virus (MOPV)) and across the target phosphodiester bond. In the previous reported structures (Yekwa *et al.*, 2017), only one metal ion was observed and the second one was transiently observed in the presence of RNA substrate (Jiang et al., 2013). The domain is specifically active against double stranded RNA in presence of Mg^{2+} and boosted in the presence of Mn^{2+} .

In this study we present the identification of a compound that could be considered as a hit compound in the development of antivirals against *Arenaviridae* 3'-5' exonuclease activity. We used an *in silico* approach including the virtual screening of a library of sorted molecules to identify a compound that inhibits MOPV and LCMV NP-exo activities *in vitro*. We further consolidated this finding with crystallographic and docking studies using MOPV NP-exo.

2. Material and Methods

2.1. Compound library

To provide valuable starting points for open virtual screening, we used a diverse and drug-like chemical library (MTiOpenScreen Diverse-lib) containing 99,288 molecules (Labbé et al., 2015). A sub-set of 10,000 ligands were screened in this study using the lead-like pre-filter selection by flexible physico-chemical criteria.

2.2. Structure-based Virtual screening

We used the structure of the C-terminal exonuclease domain of the Mopeia virus nucleoprotein (MOPV NP-exo) which was solved in complex with a Mg^{2+} ion in our group (PDB : 5LRP). An initial virtual screening was performed using 10,000 ligands of the MTi-OpenScreen Diverse-lib using the web-server (<https://bioserv.rpbs.univ-paris-diderot.fr/services/MTiOpenScreen/>). We provided the following input information (i) a pdb file of the protein structure and (ii) the center and the grid dimensions ($a=b=c=30 \text{ \AA}$) of the protein active site. The uploaded pdb file was automatically cleaned by removing all HETATMS and H-bonds using MGL Tools (Labbé et al., 2015). This screen generated a list of the top-ranked predicted binding poses and energies of 100 ligands.

2.3. Molecular Docking

The 3D structure of MOPV NP-exo (PDB: 5LRP) was energy minimized by the steepest gradient method of energy minimization followed by conjugate gradient minimization, using the MMTK and Amber packages (Cornell et al., 1995; Hinsen, 2000; Lindorff-Larsen et al., 2010). Mol2 and PDB file formats of the ligands and receptor were converted to PDBQT format using *UCSF Chimera* (Pettersen et al., 2004) prior to docking. All the water and solvent atoms of the protein were removed and the polar hydrogens and polar charges were added onto the ions and ligand prior to docking. The protein was kept rigid while the ligand was allowed to rotate and explore more flexible binding modes. Docking of the ligands onto the NP-exo MOPV was performed iteratively using AutoDock vina - version 1.1.2 (Trott and Olson, 2010). The best poses from the first round of docking were used as seeds for the second round. The grid box size was further optimized to dimensions $a = 23.2 \text{ \AA}$, $b = 25.6 \text{ \AA}$, $c = 21.2 \text{ \AA}$ thus covering the binding pocket. The default scoring function was used for docking. Binding modes of the docked complexes were obtained and sorted based on their binding energy. Ions and amino acid residues present at a distance of less than 3 \AA were considered as the binding partners of the ligands.

Geosmin synthase from *Streptomyces coelicolor* (ScGS) in complex with three Mg^{2+} ions and ALD (PDB:5DZ2) was used as a control experiment. The same protocol was applied to the 3D structure of ScGS depleted of its solvent and ALD. The ScGS - ALD binding pose resulting from our docking protocol was superimposed over the experimentally derived structure. The interaction figures representing the docked complexes have been generated using UCSF chimera.

Exploration of various possible dynamic poses of ALD in the MOPV NP-exo structure with Mn^{2+} obtained in this study (PDB:6SX8) was performed with Autodock Vina with a grid

(dimensions: $a = 29.34 \text{ \AA}$, $b = 28.71 \text{ \AA}$, $c = 28.00 \text{ \AA}$) with the ion placed in the center of the grid to allow an extensive exploration of possible poses.

2.4. Cloning, gene expression and purification of proteins

The MOPV NP-exo (residues 365-570 – NCBI #P19239) and LCMV NP-exo (residues 357-559 - #NP_694852) genes were cloned by recombination (Gateway, Invitrogen) into the pETG20A expression vector, which adds a cleavable N-terminal thioredoxin-hexahistidine tag. The accuracy of the DNA construct sequence was verified by sequencing.

Vectors were used to transform T7 Express competent *E. coli* cells (#C2566, New England Biolabs) carrying the pRARE plasmid (Novagen). Bacteria were cultured in Turbo Broth™ medium (AthenaES) at 310 K. When the $OD_{600\text{nm}}$ reached 0.6, gene expression was induced by 0.5 mM isopropyl β -D-1-thiogalactopyranoside (IPTG) and cells were incubated overnight at 290 K while agitating at 250 r.p.m. in presence of 100 μM of ZnCl_2 . Bacteria were pelleted by centrifugation and stored at 193 K.

Cell pellets were resuspended in lysis buffer (20 mM HEPES pH 7.5, 300 mM NaCl, 5 mM imidazole, 5% glycerol, 0.25 mg/ml lysozyme, 100 $\mu\text{g/ml}$ DNase, 0.1 mM phenylmethylsulfonyl fluoride and 0.1% triton X-100) at 193 K, followed by sonication. The lysate was then cleared by centrifugation at 20,000 $\times g$ at 277 K for 30 minutes. Each protein was first purified by immobilized metal affinity chromatography (IMAC) using 5 ml of HisPur™ cobalt resin (Thermo Scientific). The His-tagged proteins were recovered by using elution buffer 20 mM HEPES pH 7.5 containing 200 mM NaCl, 250 mM imidazole and 5% glycerol. The tag was cleaved by TEV protease followed by a second IMAC step removing non-cleaved protein and the His-tagged TEV protease. The final step consisted of gel filtration using a Superdex 200 column (Cytiva) in 10 mM HEPES pH 7.5, 150 mM NaCl, 3 mM MnCl_2 and 5% glycerol. The quality of both proteins was verified by SDS PAGE and mass spectrometry.

The gene of human t3' repair exonuclease 2 (hTREX2) cloned into the pLM-303 vector was kindly provided by Thomas Hollis, Wake Forest University Health Sciences, USA. This construct consists of hTREX2 as a fusion protein with maltose binding protein (MBP). The complex hTREX2-MBP was expressed in *E. coli* BL21 (DE3) pLysS cells (Novagen). Transformed cells were cultured in Luria Broth™ medium (AthenaES) at 310 K in the presence of 50 mg/ml kanamycin and 34 mg/ml chloramphenicol. When $OD_{600\text{nm}}$ reached 0.4–0.6, protein expression was induced with 1 mM IPTG; and completed overnight at 290 K. The cells were collected by centrifugation. Cell pellets were lysed by sonication in 100 mM Tris, pH 7.5 containing 300 mM NaCl, 5 mM imidazole, 5% glycerol, 0.25 mg/ml lysozyme, 50 $\mu\text{g/ml}$ DNase, 0.1% Triton X-100 and 0.1 mM EDTA at 193 K. The lysate was clarified through centrifugation at 20,000 $\times g$ at 277 K for 30 minutes. The supernatant was

harvested and loaded onto an affinity chromatography column containing 5 mL amylose resin (GE Biosciences). Protein was eluted with 50 mM Tris, pH 7.5, 200 mM NaCl, 5 mM imidazole, 5% glycerol, 0.1 mM EDTA, 1 mM DTT and 10 mM maltose. The MBP was removed by treatment with PreScission Protease™ (GE Healthcare) at 277 K for 20 h while being dialyzed in buffer comprising 50 mM Tris, pH 7.5, 150 mM NaCl, 5% glycerol, 0.1 mM EDTA and 2 mM DTT. The hTREX2 was separated from cleaved MBP by an ion exchange column (HiTrap QFF 5 ml, Cytiva) and finally purified by a size-exclusion column (HiLoad 16/60 Superdex 75, Cytiva) in 20 mM Tris, pH 7.5, 150 mM NaCl, 5% glycerol and 2 mM DTT. hTREX2 protein was concentrated to 5 mg/ml and stored at 253 K until use.

2.5. Enzymatic activity assays

2.5.1. RNA substrate

The purified (HPLC) synthetic HP4 RNA (Biomers) used as a substrate for *in vitro* assays is a stable RNA hairpin (5'-UGACGGCCCGGAAAACCGGGCC-3', $\Delta G = -14.8$ kcal/mol). The RNA was labeled at its 5' end with [γ -³²P]-ATP (Perkin-Elmer) using T4 polynucleotide kinase (New England BioLabs) according to the manufacturer's instructions.

2.5.2. DNA substrates

HPLC-grade synthetic ssDNA (20 nt, 5'-ACTGGACAAATACTCCGAGG-3') and Y shaped DNA (24 nt, 5'-TTAAGGCCCTCTTTAGGGCCAAGG-3') from Eurofins genomics were used as substrates for the *in vitro* hTREX2 assays. The DNA substrates were equally labeled with [γ -³²P]-ATP using T4 polynucleotide kinase (New England BioLabs) following manufacturer's instructions.

2.5.3. Inhibitors

Alendronate (ALD) sodium trihydrate (C₄H₁₂NaNO₇P₂ · 3 H₂O) was purchased from Sigma.

2.5.4. Exonuclease activity assay

MOPV NP-exo activity was measured with 0.25 μ M NP-exo in reaction buffer 20 mM Tris, pH 8.0 containing 5 mM MnCl₂ (or MgCl₂), 2 mM DTT, 0.1 mM EDTA and 1.5 μ M radio-labelled HP4 RNA substrate. The negative control corresponds to the same set-up without enzyme. The inhibition assays were carried out in presence of a given concentration of ALD. NP-exo, ions and inhibitor were incubated in reaction buffer at RT for 5 minutes, and the reaction was then triggered by adding radio-labeled HP4 RNA substrate followed by incubation at 310.15 K. The reaction was stopped after different time intervals (0, 5, 30 min) by adding formamide gel-loading buffer (FBD: 95 % deionized formamide, 0.1 %

bromophenol blue, 0.1 % xylene cyanol FF, 10 mM EDTA) at a ratio 2:3 (v:v, sample to FBD buffer, respectively). The products were heated at 343.15 K for 10 minutes and rapidly cooled on ice before being analyzed by denaturing PAGE using sequencing gels (20% acrylamide:bisacrylamide (19:1), 8 M urea with TTE buffer (89 mM Tris pH 8.0, 28 mM taurine (2- aminoethanesulfonic acid), 0.5 mM EDTA). RNA product bands were visualized using photo-stimulated plates and an Amersham™ Typhoon™ biomolecular imager (Cytiva). RNA degradation was quantified using the ImageQuant TL program (Cytiva). IC₅₀ values were determined using GraphPad PRISM version 7.0. Experiments were performed in triplicate.

Human TREX2 assays were carried out with 0.25 μM hTREX2 in reaction buffer 20 mM Tris, pH 7.0 containing 120 mM NaCl, pH 7.0, 5 mM MnCl₂ (or MgCl₂) and 0.5 μM of radio-labeled DNA substrates. The negative controls were carried out in absence of enzyme. The inhibition assay was done in presence of 100 μM of ALD. The reactions were started by adding DNA substrates and incubated for 30 min at 310.15 K. The reaction was stopped by adding 1.5 volumes of FBD buffer and sample were analysed as described above. Experiments were carried out in duplicates.

2.6. Protein-ligand crystallization and structure characterization

2.6.1. Crystallization

Protein was concentrated up to 15 mg/ml . The screening was performed in SwissCi-96sol plate by using buffer “PEGs Suite” and the sitting-drop vapour-diffusion method. Three different volumes of protein (300, 200 and 100 nl) were mixed with a constant volume of precipitant (100 nl) by using a nanodrop-dispensing robot (Mosquito, TTPlabtech). The crystallization plate was kept at 277 K overnight, then, was changed up to 291 K. The optimal crystallization conditions of MOPV NP-exo complexed with Mn²⁺ were obtained by mixing 200 nl or 100 nl of protein with 100 nl reservoir solution consisting of 0.1 M MES pH 6.2-6.8 with 24-26 % (m/w) PEG 8000. Once the condition with Mn²⁺ was established, crystals were soaked in several concentrations of MnCl₂ (from 1 to 2 mM) and ALD (from 1 to 4 mM) during a range of time from 5 minutes to 24 hours. The crystals were protected with a cryo-protectant consisting of 20% glycerol versus 80% reservoir solution and flash-cooled in liquid nitrogen at 100 K.

2.6.2. Data collection and structure

Diffraction data were collected on the Proxima 1 beamline at the Synchrotron Soleil (Saint-Aubin, France) with the large in-vacuum PILATUS 6M detector (Dectris, Switzerland) at a wavelength of 0.97857 Å with 0.1° oscillations, 0.097 s exposure time and also on the

ID23-1 beamline at the European Synchrotron Radiation Facility (ESRF), Grenoble, France using the large in-vacuum PILATUS 6M-F detector (Dectris, Switzerland) at a wavelength of 0.9787 Å with 0.1° oscillation, 0.037 s exposure time and a temperature of 100 K. Collected data were subsequently processed using *autoProc* toolbox (Vonrhein et al., 2011). The data were integrated using the program *XDS* (Kabsch, 2010), then analyzed with *POINTLESS* (Evans, 2006) and scaled with *AIMLESS* (Evans and Murshudov, 2013). The structure was solved using the MOPV NP-exo as a search model (PDB:5LS4 ; (Yekwa et al., 2017)). The search model was prepared by removing all ligands, metallic ions and water molecules from the original structure. Phases were obtained by molecular replacement using *Phaser* (McCoy et al., 2007). Refinement was performed by successive and alternate rounds of using *BUSTER* (Bricogne et al., 2018) or PHENIX and model improvement using *COOT* (Emsley and Cowtan, 2004). The structures were validated using *MolProbity* (Williams et al., 2018) and *PROCHECK* (Laskowski et al., 1993). Structural analysis was performed using *UCSF Chimera* (Pettersen et al., 2004). The PDB X-ray structure was validated and deposited in Protein Data Bank. Data collection, refinement statistics and accession numbers are shown in Table 1.

3. Results

3.1. Structure-based virtual screening and molecular docking

The high resolution crystal structure of MOPV NP-exo (1.9 Å) complexed with Mg²⁺ (PDB: 5LRP) was used for this study. The active site comprises five catalytic residues D390, E392, D534, D467 and H529 which form an acidic cavity. Three of these residues directly coordinate one of the catalytic ions, in this case a Mg²⁺ as shown in Fig. 1(a). In order to identify ligands with high affinity for MOPV NP-exo with the aim of inhibiting its 3'-5' exonuclease activity, we performed a structure-based virtual screen of a total of 10,000 ligands from the MTi-Openscreen Diverse-lib (see Material and methods). The diverse library is composed of the sampling of 12 chemical libraries from PubChem BioAssay Database containing drug-like compound collection. Our initial structure-based virtual screening using the MTi-Openscreen server generated a total of 100 ligands that could interact with MOPV NP-exo at its active site. The ligands were ranked according to their predicted binding energies with the lowest predicted binding energy of -9.44 kcal/mol. Tables S1 and S2 show the predicted binding energies and physicochemical properties as well as the structural formulae of the top ten hits.

Manual inspection of this list of the top ten 10 ligand hits allowed us to identify the presence of a geminal bisphosphonate molecule, alendronate (ALD), which in its pose mimics

the phosphate of RNA substrates as shown in Fig. 1(b-c). Structurally, ALD is a chemically stable derivative of inorganic pyrophosphate (PPi).

Using Autodock Vina we re-docked the ALD compound with one or two Mg^{2+} ions in the catalytic site of MOPV NP-exo. Since there is no crystal structure of an arenavirus NP-exo domain in complex with ALD to the best of our knowledge, in order to access the efficiency of prediction of our model, we validated the docking protocol on the structure of geosmin synthase from *Streptomyces coelicolor* (ScGS) complexed with three Mg^{2+} ions and ALD (Fig. S1(a) and (b)). We obtained two models (Fig S1(c), (d) and (e)) with an overall root mean square deviations (rmsd) between the two ALD molecules between 1.68 Å and 2.07 Å, but a rmsd between 0.68 Å and 1.28 Å at the phosphonate level (Fig. S1(f)). We concluded that our docking protocol can predict conformations that are in agreement with experimentally determined structures.

The best ALD binding energy obtained after Autodock Vina is -7.62 kcal/mol, which is consistent with the result from the screening -7.6 kcal/mol, Table S2). The binding mode of ALD with MOPV NP-exo and its interactions with the Mg^{2+} ion in site A (present in PDB:5LRP) as well as the active site residues is shown in Fig. 1(c). The structure of ALD contains an alkyl chain of 5 C, substituted by an hydroxyl group and terminated by a primary amine and two geminal phosphonate groups $PO(O^-)_2$ negatively-charged that are able to establish electrostatic interaction. The phosphonate groups establish hydrogen bond interactions with D534 (2.4 Å), D390 (2.7 Å), I391 (3.0 Å) and direct polar interactions with E392 (2.5 Å and 3.0 Å) and the Mg^{2+} ion (1.7 Å and 1.9 Å). As the active site of *Arenaviridae* NP-exo can harbour two catalytic metal ions, a model of MOPV NP-exo with two Mg^{2+} ions was generated based on the homologous structure of a dsRNA bound to LASV NP-exo containing two Mn^{2+} ions (PDB: 4GV9). The dsRNA from the original crystal structure was removed while conserving the second Mg^{2+} ion within the MOPV model that was then used for docking. As Fig. 1(d) shows, in the presence of two Mg^{2+} ions, ALD positions itself in such a way that the two phosphonate groups establish polar interactions with both metal ions. In addition to the residues cited earlier it also makes polar interactions with the main chain of G463 and G464. The binding energy of the best ALD pose in the MOPV NP-exo model with two metal ions (-16.7 kcal/mol) is approximately two times lower compared to that of the best pose within the model having a single metal ion (-7.62 kcal/mol).

3.2. Alendronate inhibits the 3'-5' activity of MOPV NP-exo and LCMV NP-exo in presence of Mn²⁺ ions

As ALD is easily available commercially we decided to evaluate its ability to inhibit the 3'-5' exonuclease activity. The method is based on the enzyme's ability to hydrolyze the 22-nt hairpin RNA HP4 that has been radiolabeled at its 5'-end and whose 3'-end is engaged in the hairpin. (dsRNA Fig. 2(a)). The effect of 100 μM ALD in presence of 5 mM Mg²⁺ or Mn²⁺ as catalytic ion was tested with MOPV NP-exo. Fig. 2(a) shows that dsRNA HP4 is degraded in presence of both metal ions. The substrate band disappears after 5 min and degradation proceeds further up to 30 min. ALD does not inhibit the dsRNA hydrolysis in the presence of Mg²⁺ but inhibits degradation completely in the presence of Mn²⁺. Interestingly, the same Mn²⁺-ion-dependent inhibition is observed when ssDNA and Y-shaped DNA was degraded by recombinant human TREX2 in presence of Mg²⁺ or Mn²⁺ (Fig. 2(b)). Here we also observed inhibition by 100 μM ALD in the presence of Mn²⁺.

Subsequently, MOPV NP-exo or LCMV NP-exo and the dsRNA HP4 were incubated in the presence Mn²⁺ with increasing concentrations of ALD (10 to 250 μM). Fig. 2(c) and (d) show that both enzymes are inhibited; and that inhibition is almost complete at 150 μM ALD. In order to determine IC₅₀ values both reactions were then done in triplicates in the presence of 10, 25, 50, 75, 100, 125, 150 and 200 μM ALD. Quantitative comparison of the disappearance of the substrate band after 5-min incubation in comparison to the absence of ALD was used to calculate the percentage of activity at a certain ALD concentration (Fig. 2(e) and (f)). IC₅₀ values were determined by GraphPad Prism to be 65.9 +/- 1.7 μM ALD and 68.6 +/- 4.2 μM ALD for MOPV NP-exo or LCMV NP-exo, respectively.

In conclusion, although we expected from our screening and docking approach that ALD could inhibit arenavirus NP-exo activity in presence of Mg²⁺ ions, we obtained a Mn²⁺-specific inhibition with moderate IC₅₀ values.

3.3. Crystal Structures of the MOPV NP-Exo complexed with Mn and soaked with ALD.

In order to structurally investigate the mechanism of action of ALD to inhibit the 3'-5' exonuclease activity in presence of Mn²⁺ ions, and see if ALD could fix the second catalytic ion, we crystallized MOPV NP-Exo complexed with Mn²⁺ and soaked the crystals with ALD applying different soaking times (6 min to over night). We obtained four structures, which are listed in Table 1. The first structure is complexed with one Mn²⁺ and represent our reference structure (PDB:6SX8, Fig 3(a)). Its general structure and ion location are similar to the ones reported with Mg²⁺ and Ca²⁺ (Yekwa *et al.*, 2017). MOPV NP-exo in complex with Mn²⁺ consists of 6 mixed strands forming a central β -sheet sandwiched by 3 α -helices on one side and 5 α -helices on the opposite side. Two flexible regions are present within the structure. Two anti-parallel strands form a 'basic loop' (residues 514-526) near the catalytic pocket; and

the C-terminal arm (residues 549-570) extends away from the protein core. The MOPV NP-exo structure presents a structural conserved Zinc-binding domain. The Zn^{2+} metal ion is coordinated by E400, C507, H510 and C530. The Mn^{2+} ion is coordinated by three catalytic residues D390, E392, D534 and three H_2O molecules (Fig. 3(b)). The presence of Mn^{2+} and Zn^{2+} ions in the crystal were confirmed by an X-ray fluorescent scan (Fig. S2). The other three structures were obtained after soaking crystals with ALD for 6 min (PDB:6T6L), 12 min (PDB:6T2A) and overnight (PDB:6SY8). The overall structures are not changed by the soaking except for the fact that the basic loop is clearly defined in all three structures issued from soaking with ALD in contrast to the one complexed with Mn^{2+} indicating that ALD contributes to lower the energy of this structural element. The structure of the Zn-binding domain and the four residues forming the conserved Zinc-binding site are not affected by the soaking with ALD. In the active site, the density around the water molecules and the ion are significantly weakened indicating a gradual depletion of the ion in the structure. The three water molecules are still present after 6 minutes of soaking (Fig. 3(c)) but start to disappear after 12 minutes (Fig. 3(d)). The Mn^{2+} ion is still present in the structures but its occupancy was refined at 52 % and 34 %, respectively to reflect the disappearance. This is indicative that in presence of ALD there is a depletion of the Mn^{2+} in the structure. Finally, after 40 min (not presented) or overnight soaking (Fig. 3(e)) we observed no density in the catalytic site reflecting the complete disappearance of the Mn^{2+} ion. During refinement we observed positive density around the Mn^{2+} ion larger than a regular water molecule (Fig S3(a)) but we were not able to refine with an ALD molecule, indicating that the process of ALD binding to MOPV NP-exo complexed to Mn^{2+} is extremely dynamic and that ALD is not stabilized by strong interactions with the protein.

Using our structural data we re-docked ALD, taking into consideration the position of the Mn^{2+} ion, the coordinated water molecules (Fig. 4(a)), and a positive blob of unrefined density observed in the structure after soaking with ALD (6 min) Fig S3(a). After applying our Autodock Vina protocol we obtained a series of possible ALD poses (Fig S3(b) left). Molecules for which at least two oxygens of ALD overlap with the observed position of water molecule and compatible with the observed unrefined density lead to select three poses (Fig 4(b) and Fig S3(b) right). These poses allow to propose that oxygen atoms of the ALD phosphonates are displacing the coordinated water molecules, by doing so they weaken the affinity of the ion towards the protein, allowing its sequestration by the ALD.

In conclusion, our structure-function analysis of MOPV NP-exo with Mn^{2+} and ALD indicate that the inhibitory effect of ALD is specific to Mn^{2+} through specific metal chelation.

4. Discussion

Several pieces of evidence demonstrate that metal-dependent enzymes are important targets for antiviral discovery (Carcelli *et al.*, 2017; DiScipio *et al.*, 2022). The chelation of metal ion co-factors is therefore an interesting and approved strategy for the development of novel antiviral therapy (Rogolino *et al.*, 2012). The arenavirus 3'-5' exonuclease is a divalent metal dependent enzyme that requires Mn^{2+} (or Mg^{2+}) as a co-factor. This enzyme degrades immunogenic dsRNA, a process thought to be used by arenaviruses to suppress type I interferon induction (Hastie *et al.*, 2011a; Jiang *et al.*, 2013; Qi *et al.*, 2010). It was also suggested that this 3'-5' exonuclease might be playing an important role during RNA replication (Huang *et al.*, 2015). Moreover, the catalytic tetrad DEDD is completely conserved among arenaviruses (Hastie *et al.*, 2011b) thus making this enzyme an interesting target for the development of broad spectrum antivirals across the *Arenaviridae* family.

Here we used a structure-based virtual screening and molecular docking approach to identifying a ligand that inhibits the 3'-5' exonuclease activity of two arenavirus NP-exo domains in a Mn^{2+} -specific manner *in vitro*. Among the ten best ligands coming out of screening, we chose one compound based on its ability to bind through ion interaction at the active site thus preventing the binding of the phosphate of the enzyme's RNA substrate. That choice was driven by our knowledge of the targeted active site, the mechanism of RNA hydrolysis by the arenavirus 3'-5' exonuclease and the availability of the co-crystal structure of a dsRNA bound to the LASV exonuclease domain (Yekwa *et al.*, 2019; Jiang *et al.*, 2013).

We soaked the compound to co-crystallize it within the NP-exo domain. Contrary to our expectations ALD did not mimic the working substrate condition since failed to retain a second ion. The complex with ALD did not form, but we observed the depletion of the ion in the catalytic site over time. These results allow to propose that ALD does not pre bind an ion prior coming to the catalytic site. We know from the structure of geosmin synthase that ALD is able to interact with up to three metal ions at once. In the case of MOPV NP-exo we observe a more dynamic mechanism. In our simulation, the phosphonate groups of ALD seem to establish polar interactions specifically with the catalytic Mn^{2+} ion in place of the water molecules. These interactions are in agreement with those seen between the negatively charged phosphate of the RNA substrate and the Mn^{2+} in the co-crystal structure of the dsRNA bound to the LASV NP-exo domain (Jiang *et al.*, 2013). From the structural study ALD inhibits the 3'-5' exonuclease activity through metal ion chelation and neither steric hindrance nor competition with the substrate for the active site.

According to our *in vitro* analysis, ALD inhibits the activity of MOPV NP-exo and LCMV NP-exo with values in the micromolar range. Interestingly, it has no effect in presence of Mg^{2+} but only inhibits the enzyme in presence of Mn^{2+} . It is not the first time that such

discrimination of a compound towards metallic ion is being observed in nucleases (Saez-Ayala *et al.*, 2019), and this reinforces our consideration that ALD inhibits the 3'-5' exonuclease activity through specific ion chelation. Control experiments using human TREX2 (hTREX2) shows similar ion dependency effect on two different types of DNA substrate. It was previously demonstrated that few viral nucleases such as the one of Influenza virus use Mn^{2+} (Crépin *et al.*, 2010) while cellular enzymes as hTREX2 are more prone to use Mg^{2+} (de Silva *et al.*, 2009). In this context, it would be possible to consider *in vivo* a limited effect on hTREX2 even at high concentration of ALD. That molecule belongs to the bisphosphonate family (BP). They are pyrophosphate analogues and are inhibitors of mevalonate pathway, mainly targeting the Farnesyl pyrophosphate synthase (FDPS)(Rondeau *et al.*, 2006), thus preventing prenylation of key signaling proteins, the GTPases : Ras, Rho, and Rab (Koshimune *et al.*, 2007; Rogers *et al.*, 2011). Moreover BPs are inhibitors of bone resorption (Fleisch, 1991). Also, BPs are used to cure the skeletal complications (Goffinet *et al.*, 2006; Van Acker *et al.*, 2016). Nitrogen containing bisphosphonates (such as ALD) have been used for the treatment of osteoporosis and tumor related hypercalcemia (Reszka and Rodan, 2004). There has been increasing evidence that BPs can inhibit proliferation and induce apoptosis in a variety of human tumor cells like myeloma, breast, pancreas, and prostate under various conditions (Senaratne *et al.*, 2000; Takahashi *et al.*, 2001; Virtanen *et al.*, 2002). To our knowledge there has been no previous report of BP in used in antiviral therapy. Other pyrophosphate analogues such as phosphonoformic acid (PFA, Foscarnet) and phosphonoacetic acid (PAA) are known to be potent inhibitor of Herpes virus DNA polymerases (Eriksson *et al.*, 1982). Foscarnet is a broad spectrum antiviral used for the treatment of human cytomegalovirus and it also inhibits HIV-reverse transcriptase (Marchand *et al.*, 2007). It inhibits DNA polymerases by trapping the polymerase-DNA complex in its untranslocated form. A structural study on a chimeric DNA polymerase complexed with foscarnet revealed its mode of binding within the active site, showing that foscarnet chelates metal ions while interacting with conserved residues of the finger domain which are critical for catalysis (Zahn *et al.*, 2011). Even if ALD is not a potent viral inhibitor this study shows that it is a moderate inhibitor *in vitro* and proposes that pyrophosphate analogues might constitute promising lead molecules for the development of antivirals against the arenavirus exonuclease. Bisphosphonates are known to be very stable compounds in biological fluids due to their chemical structure which makes them resistant to enzymatic hydrolysis by pyrophosphatases (e.g. acid phosphatase, alkaline phosphatase) (Russell, 2006).

In a strategy against *Arenaviridae*, the idea of having a molecule targeting the viral nuclease to restore even partially the innate immune response is an interesting lead to follow (Saez-Ayala *et al.*, 2019). It would break the persistence cycle of infection, allowing the cells to have a better chance to defend. It would also be interesting to consider this type of

molecule in combination with other potential candidate targeting other aspects of the viral life cycle, such as the replication inhibitor T-705 (Mendenhall, Russell, Smee *et al.*, 2011; Mendenhall, Russell, Juelich *et al.*, 2011).

5. Conclusion

We report four crystallographic structures of the MOPV Exo: one in complex with a Mn^{2+} ion and three with its disappearance overtime in presence of ALD. We have demonstrated the efficacy of ALD as an *in vitro* inhibitor of the MOPV NP-exo and LCMV NP-exo two model viruses for the *Arenaviridae*. The data shows that the mechanism of inhibition is through specific ion chelation and not steric hindrance or competition with the substrate for the active site. Further *in vivo* and screening experiments are needed to verify that ALD analogues or Mn^{2+} chelators could be used as a lead molecule for the development of an antiviral. Nevertheless our study suggests that bisphosphonate could be a promising scaffold that can be optimized to develop improved inhibitors of the 3'-5' exonuclease of arenaviruses.

Figure 1 Screening and docking experiments against MOPV NP-Exo. (a) The crystal structure of MOPV NP-Exo used for docking studies (PDB:5LRP) presented as a ribbon diagram of the protein with helices in blue, β -strands in pink and loops in cyan. Active site residues are shown with their side chains in sticks (C-atoms in grey, O-atoms in red and N-atoms in blue). The coordination of the Mg^{2+} ion (green sphere) is also illustrated. The expanded square corresponds to the red-green box shown on the molecular surface representation of the MOPV NP-exo structure. It represents the grid box used to define the docking space covering the entire active site. (b) Interactions of reference of RNA with the catalytic site of LASV and a single Mn^{2+} ion (purple sphere) (PDB:4GV6). (c) Interactions of ALD inside the MOPV NP-exo active site in the presence of a single Mg^{2+} ion obtained by Autodock Vina. (d) ALD interaction with the MOPV NP-exo model containing two Mg^{2+} ions after Autodock Vina.

Figure 2 ALD inhibition of the 3'-5' exonuclease activity. (a) MOPV NP-Exo was incubated with HP4 dsRNA in the absence or presence of catalytic ions Mg^{2+} or Mn^{2+} and a fixed concentration of ALD (100 μ M). Reaction samples were taken after time intervals of 0, 5 and 30 minutes (min). The products were analyzed on Urea-PAGE and visualized by autoradiography. (b) Inhibition of human TREX2 activity in presence of 100 μ M of ALD. Left panel: Inhibition of hTREX2 activity on single-stranded DNA (ssDNA); right panel: inhibition of the hTREX2 activity using Y-shaped DNA with 4-nt-long 3'- and 5'-overhangs. (c) and (d) show representative gels showing the effect of ALD on the exonuclease activity of MOPV NP-exo and LCMV NP-exo, respectively. (e) and (f) are dose response curves from which IC_{50} values were calculated. For IC_{50} determination, the percentage of activity was measured by quantifying total product formed after 5 minutes. IC_{50} values were then determined by fitting the dose response curves. Reactions were done in triplicates.

Figure 3 Crystal structure of MOPV NP-Exo complexed with Mn^{2+} and soaked in presence of ALD. (a) Ribbon representation of MOPV NP-exo structure complexed with Mn^{2+} (PDB:6SX8). Mn^{2+} is represented as a purple sphere and coordinated by three water molecules (red spheres). The protein structure color code follows the one in Fig 1. Catalytic residues are labeled. Three of the residues coordinating the structural Zn^{2+} ion (grey sphere) are also shown with their side chains in sticks. (b) Zoom of the Mn^{2+} ion in the active site of MOPV NP-exo complexed with Mn^{2+} . The theoretical Mn^{2+} coordination by the catalytic residues and water molecules are illustrated by yellow arrows. (c to e) Same view as (b) presenting a 2Fo-Fc map corresponding to the metal ion-binding site contoured at 1.3σ at different soaking time *i.e.* (c) time 6 minutes (PDB:6T6L), (d) time 12 minutes (PDB:6T2A), (e) overnight (PDB:6SY8).

Figure 4 Exploration of potential ALD poses resulting from docking experiment using the crystal structure of MOPV NP-Exo complexed with Mn^{2+} . (a) Molecular surface representation of the MOPV NP-Exo structure complexed with Mn^{2+} represented as a purple sphere and coordinated by three water molecules (red spheres). The positioning of the water molecules serves as a reference for potential binding modes. Their distances from the ion are given in the zoom (lower panel). (b) Molecular surface representation of the MOPV NP-Exo structure complexed with Mn^{2+} depleted of water molecules. The orange box corresponds to the relaxed docking grid encompassing the active site in which the ion is at its center. The three best poses compatible with the observed unrefined density (Fig. S3) and the position of the water molecules. The given distances are compatible with the observed distances with coordinated waters.

Table 1 Data processing, structure solution and refinement.

Data processing				
	MOPV NP-Exo	MOPV NP-Exo	MOPV NP-Exo	MOPV NP-Exo
	complexed with	soaked with ALD	soaked with ALD	soaked with ALD
	Mn ²⁺	(6 min)	(12 min)	(overnight)
Wavelength (Å)	0.9786	0.9724	0.972	0.9786
Space group	P 1 2 1	C 1 2 1	P 1 2 1	P 1 2 1
- a, b, c (Å)	45.54, 38.01,	133.21, 111.34,	45.59 37.97,	45.85, 38.29,
- α, β, γ (°)	137.23	49.15	137.38 90.00,	137.31
	90.00, 92.94, 90.00	90.00, 104.17,	93.31, 90.00	90.00, 92.63, 90.00
		90.00		
Resolution range	38.82 - 1.8	44.66 - 1.76	42.48 - 2.0	33.13 - 2.08
(Å)	(1.864 - 1.8)	(1.82 - 1.76)	(2.07 - 2.0)	(2.16 - 2.08)
Total No. of reflections	159861 (15626)	242240 (24702)	90988 (6843)	154341 (15620)
No. of unique reflections	43794 (4304)	67897 (6824)	29975 (2211)	28850 (2855)
Completeness (%)	98.69 (97.97)	98.27 (98.88)	92.75 (69.22)	98.88 (98.40)
Multiplicity	3.7 (3.6)	3.6 (3.6)	3.0 (3.1)	5.3 (5.5)
I/σ(I)	14.99 (2.99)	10.54 (2.31)	23.73 (6.53)	12.85 (2.28)
R _{meas}	0.04673 (0.405)	0.08419 (0.5895)	0.03108 (0.1421)	0.1177 (0.9836)
CC1/2	0.999 (0.976)	0.996 (0.8)	0.999 (0.995)	0.998 (0.95)
Wilson B-factor (Å)	27.2	21.79	18.4	35.3
Structure solution & refinement				
No. of reflections, working set	43526 (4243)	67834 (6822)	29970 (2208)	28680 (2832)
No. of reflections, test set (%)	2195 (217), 5.0 %	3468 (330), 5.21 %	1983 (142), 6.6 %	1346 (124), 4.7 %
R _{cryst}	0.21	0.1908 (0.2394)	0.23	0.25
R _{free}	0.25	0.2161 (0.2817)	0.27	0.28
No. of non-H atoms	3417	5721	3282	3302
-Protein	3183	4926	3151	3183
-Ligand	4	6	11	2
-Water	230	789	120	117
R.m.s. deviations				
-Bonds (Å)	0.007	0.009	0.007	0.014
-Angles (°)	1.18	1.38	0.81	1.61
Average B-factors (Å ²)				
-Protein	43.00	29.27	25.97	53.84
-Ligand	43.76	28.03	25.39	53.96
-Water	38.10	20.22	41.34	40.17
	47.04	37.11	39.87	50.75
Ramachandran Plot				
-Favoured (%)	97.43	96.89	97.93	97.43
-Allowed (%)	2.57	3.11	2.07	2.57
-Outliers (%)	0.00	0.00	0.00	0.00
Clashcore	6.77	6.72	6.83	4.10
PDB code	6SX8	6T6L	6T2A	6SY8

Statistics for the highest-resolution shell are shown in parentheses.

Supporting Figures and Table legends.

Figure S1. Geosmin synthase original structure versus exploration by Autodock Vina. (a) Crystal structure of geosmin synthase from *Streptomyces coelicolor* (ScGS) in complex with three Mg^{2+} ions and ALD (PDB:5DZ2). The protein structure is represented as a ribbon diagram with active site residues coordinating the Mg^{2+} ions (green spheres) shown in sticks. (b) Zoom of the observed coordination of Mg^{2+} ions by ALD in (PDB:5DZ2) (c) Resulting docking positions of ALD in the crystal structure of ScGS in complex with three Mg^{2+} ions with AutoDock Vina (beige and green molecules) (d and e) Zoom of the observed coordination of Mg^{2+} ions by ALD resulting from the docking (F) Superposition of the observed ALD (cyan) versus the resulting docking positions (beige and green).

Figure S2. X-ray fluorescence scan to confirm the presence of Mn^{2+} . Scan realized on Proxima 1 synchrotron beam-line directly on the exposed crystal. It shows the presence of peaks corresponding to Mn^{2+} and Zn^{2+} .

Figure S3. Use of experimental data for best pose selection. (a) Observed positive density (green) of FO-FC map spiking around the ion during refinement of soaked ALD (6min). As this density only appears in soaked crystals we assume that it is ghost signal of ALD and used that density to choose the best pose proposed by the docking experiment. The left panel is a view of the overall catalytic site; the right panel is the a zoomed view rotated by 45° from the left panel and centered on the Mn^{2+} ion. (b) Left : All poses resulting from the docking experiment (-4.2 to -4.7 kcal/mol). Right: Selected 3 poses compatible with the observed density (-4.6 kcal/mol).

Table S1 : Predicted binding energy and physico-chemical properties of ten best hits from docking against MOPV NP-Exo

Table S2 : Structural formula of top ten hits from docking against MOPV NP-Exo

AcknowledgementsFunding - This work was supported by ANR grants ArenaBunya-L (ANR-11-BSV8-0019) and PANUVI (ANR-18-ASTR-0010-01), the French Infrastructure for Integrated Structural Biology (FRISBI) (ANR-10-INSB-05-01) ; as well as by the Fondation pour la Recherche Médicale (FRM), the Fondation Infection Méditerranée, the SILVER Large Scale Collaborative Project (grant agreement n° 260644) of the European Union 7th Framework.

Acknowledgements - The authors want to thank Dr. Thomas Hollis for providing the plasmid and purification conditions of the Human TREX2 3'-5'-exonuclease. The authors thank synchrotrons SOLEIL beamline Proxima-1 and ESRF beamlines ID23-1 for allocation of time and support during data collection.

References

- Van Acker, H. H., Anguille, S., Willems, Y., Smits, E. L. & Van Tendeloo, V. F. (2016). *Pharmacology & Therapeutics*. **158**, 24–40.
- Bowen, M. D., Peters, C. J. & Nichol, S. T. (1997). *Molecular Phylogenetics and Evolution*. **8**, 301–316.
- Bricogne, G., Blanc, E., Brandl, M., Flensburg, C., Keller, P., Paciorek, P., Roversi, P., Sharff, A., Smart, O., Vonrhein, C. & Womack, T. (2018).
- Briese, T., Paweska, J. T., McMullan, L. K., Hutchison, S. K., Street, C., Palacios, G., Khristova, M. L., Weyer, J., Swanepoel, R., Egholm, M., Nichol, S. T. & Lipkin, W. I. (2009). *PLoS Pathogens*. **5**, e1000455.
- Buchmeier, M. J., de la Torre, J.-C., Peters, C. J. & Torre, J. D. (2007). *Fields Virology*, Vol. II, edited by D.M. Knipe & P.M. Howley, pp. 1791–1827. Philadelphia, PA, USA: Lippincott Williams & Wilkins.
- Carcelli, M., Rogolino, D., Gatti, A., Pala, N., Corona, A., Caredda, A., Tramontano, E., Pannecouque, C., Naesens, L. & Esposito, F. (2017). *Front. Microbiol.* **8**,
- Cornell, W. D., Cieplak, P., Bayly, C. I., Gould, I. R., Merz, K. M., Ferguson, D. M., Spellmeyer, D. C., Fox, T., Caldwell, J. W. & Kollman, P. A. (1995). *Journal of the American Chemical Society*. **117**, 5179–5197.
- Crépin, T., Dias, A., Palencia, A., Swale, C., Cusack, S. & Ruigrok, R. W. H. (2010). *J Virol.* **84**, 9096–9104.
- DiScipio, K. A., Weerasooriya, S., Szczepaniak, R., Hazeen, A., Wright, L. R., Wright, D. L. & Weller, S. K. (2022). *MBio*. **13**, e03226-21.
- Emsley, P. & Cowtan, K. (2004). *Acta Crystallographica. Section D, Biological Crystallography*. **60**, 2126–2132.
- Eriksson, B., Oberg, B. & Wahren, B. (1982). *Biochimica Et Biophysica Acta*. **696**, 115–123.
- Evans, P. (2006). *Acta Crystallographica. Section D, Biological Crystallography*. **62**, 72–82.
- Evans, P. R. & Murshudov, G. N. (2013). *Acta Crystallographica Section D: Biological Crystallography*. **69**, 1204–1214.
- Ferron, F., Weber, F., de la Torre, J. C. & Reguera, J. (2017). *Virus Research*. 1–17.
- Fleisch, H. (1991). *Drugs*. **42**, 919–944.
- Goffinet, M., Thoulouzan, M., Pradines, A., Lajoie-Mazenc, I., Weinbaum, C., Faye, J. C. & Séronie-Vivien, S. (2006). *BMC Cancer*. **6**, 60.
- Günther, S. & Lenz, O. (2004). *Critical Reviews in Clinical Laboratory Sciences*. **41**, 339–390.

- Hastie, K. M., Kimberlin, C. R., Zandonatti, M. A., MacRae, I. J. & Saphire, E. O. (2011). *Proceedings of the National Academy of Sciences of the United States of America*. **108**, 2396–2401.
- Hastie, K. M., Liu, T., Li, S., King, L. B., Ngo, N., Zandonatti, M. a, Woods, V. L., de la Torre, J. C. & Saphire, E. O. (2011). *Proceedings of the National Academy of Sciences of the United States of America*. **108**, 19365–19370.
- Hinsen, K. (2000). *Journal of Computational Chemistry*. **21**, 79–85.
- Huang, Q., Shao, J., Lan, S., Zhou, Y., Xing, J., Dong, C., Liang, Y. & Ly, H. (2015). *J. Virol.* **89**, 6595–6607.
- Jiang, X., Huang, Q., Wang, W., Dong, H., Ly, H., Liang, Y. & Dong, C. (2013). *The Journal of Biological Chemistry*. **288**, 16949–16959.
- Kabsch, W. (2010). *Acta Crystallographica. Section D, Biological Crystallography*. **66**, 125–132.
- Koshimune, R., Aoe, M., Toyooka, S., Hara, F., Ouchida, M., Tokumo, M., Sano, Y., Date, H. & Shimizu, N. (2007). *BMC Cancer*. **7**, 8.
- Labbé, C. M., Rey, J., Lagorce, D., Vavruša, M., Becot, J., Sperandio, O., Villoutreix, B. O., Tufféry, P. & Miteva, M. A. (2015). *Nucleic Acids Research*. **43**, W448-454.
- Laskowski, R. A., MacArthur, M. W., Moss, D. S. & Thornton, J. M. (1993). *Journal of Applied Crystallography*. **26**, 283–291.
- Lindorff-Larsen, K., Piana, S., Palmo, K., Maragakis, P., Klepeis, J. L., Dror, R. O. & Shaw, D. E. (2010). *Proteins: Structure, Function and Bioinformatics*. **78**, 1950–1958.
- Marchand, B., Tchesnokov, E. P. & Götte, M. (2007). *The Journal of Biological Chemistry*. **282**, 3337–3346.
- McCoy, A. J., Grosse-Kunstleve, R. W., Adams, P. D., Winn, M. D., Storoni, L. C. & Read, R. J. (2007). *Journal of Applied Crystallography*. **40**, 658–674.
- Mendenhall, M., Russell, A., Juelich, T., Messina, E. L., Smee, D. F., Freiberg, A. N., Holbrook, M. R., Furuta, Y., de la Torre, J.-C., Nunberg, J. H. & Gowen, B. B. (2011). *Antimicrob. Agents Chemother.* **55**, 782–787.
- Mendenhall, M., Russell, A., Smee, D. F., Hall, J. O., Skirpstunas, R., Furuta, Y. & Gowen, B. B. (2011). *PLoS Negl Trop Dis*. **5**, e1342.
- Meyer, B. & Ly, H. (2016). *Journal of Virology*. **90**, 3810–3818.
- Mofolorunsho, K. C. (2016). *Pan Afr Med J*. **23**,.
- Morin, B., Coutard, B., Lelke, M., Ferron, F., Kerber, R., Jamal, S., Frangeul, A., Baronti, C., Charrel, R., De Lamballerie, X., Vonnrhein, C., Lescar, J., Bricogne, G., Günther, S. & Canard, B. (2010). *PLoS Pathogens*. **6**, e1001038.
- Peterson, A. T., Moses, L. M. & Bausch, D. G. (2014). *PLoS ONE*. **9**, e100711.
- Pettersen, E. F., Goddard, T. D., Huang, C. C., Couch, G. S., Greenblatt, D. M., Meng, E. C. & Ferrin, T. E. (2004). *Journal of Computational Chemistry*. **25**, 1605–1612.
- Pinschewer, D. D., Perez, M. & de la Torre, J. C. (2003). *Journal of Virology*. **77**, 3882–3887.
- Qi, X., Lan, S., Wang, W., Schelde, L. M., Dong, H., Wallat, G. D., Ly, H., Liang, Y. & Dong, C. (2010). *Nature*. **468**, 779–783.
- Rawls, W. E., Chan, M. A. & Gee, S. R. (1981). *Canadian Journal of Microbiology*. **27**, 568–574.

- Reszka, A. A. & Rodan, G. A. (2004). *Mini Reviews in Medicinal Chemistry*. **4**, 711–719.
- Rogers, M. J., Crockett, J. C., Coxon, F. P. & Mänkkänen, J. (2011). *Bone*. **49**, 34–41.
- Rogolino, D., Carcelli, M., Sechi, M. & Neamati, N. (2012). *Coordination Chemistry Reviews*. **256**, 3063–3086.
- Rondeau, J.-M., Bitsch, F., Bourgier, E., Geiser, M., Hemmig, R., Kroemer, M., Lehmann, S., Ramage, P., Rieffel, S., Strauss, A., Green, J. R. & Jahnke, W. (2006). *ChemMedChem*. **1**, 267–273.
- Russell, R. G. G. (2006). *Ann N Y Acad Sci*. **1068**, 367–401.
- Saez-Ayala, M., Laban Yekwa, E., Mondielli, C., Roux, L., Hernandez, S., Bailly, F., Cotelle, P., Rogolino, D., Canard, B., Ferron, F. & Alvarez, K. (2019). *Antiviral Res*. **162**, 79–89.
- Senaratne, S. G., Pirianov, G., Mansi, J. L., Arnett, T. R. & Colston, K. W. (2000). *British Journal of Cancer*. **82**, 1459–1468.
- de Silva, U., Perrino, F. W. & Hollis, T. (2009). *Nucleic Acids Res*. **37**, 2411–2417.
- Steitz, T. a & Steitz, J. a (1993). *Proceedings of the National Academy of Sciences of the United States of America*. **90**, 6498–6502.
- Takahashi, R., Shimazaki, C., Inaba, T., Okano, A., Hatsuse, M., Okamoto, A., Hirai, H., Ashihara, E. & Nakagawa, M. (2001). *Leukemia Research*. **25**, 77–83.
- Trott, O. & Olson, A. J. (2010). *Journal of Computational Chemistry*. **31**, 455–461.
- Virtanen, S. S., Väänänen, H. K., Härkänen, P. L. & Lakkakorpi, P. T. (2002). *Cancer Research*. **62**, 2708–2714.
- Vonrhein, C., Flensburg, C., Keller, P., Sharff, A., Smart, O., Paciorek, W., Womack, T. & Bricogne, G. (2011). *Acta Crystallographica Section D: Biological Crystallography*. **67**, 293–302.
- WHO (2016a). WHO | Lassa Fever – Germany World Health Organization.
- WHO (2016b). WHO | Lassa Fever – Liberia World Health Organization.
- WHO (2016c). WHO | Lassa fever – Sweden World Health Organization.
- WHO (2017). WHO | Lassa Fever – Benin, Togo and Burkina Faso World Health Organization.
- WHO (2018). WHO | Lassa Fever – Nigeria World Health Organization.
- WHO (2022). Lassa Fever – Nigeria.
- Williams, C. J., Headd, J. J., Moriarty, N. W., Prisant, M. G., Videau, L. L., Deis, L. N., Verma, V., Keedy, D. A., Hintze, B. J., Chen, V. B., Jain, S., Lewis, S. M., Arendall, W. B., Snoeyink, J., Adams, P. D., Lovell, S. C., Richardson, J. S. & Richardson, D. C. (2018). *Protein Science*. **27**, 293–315.
- Xing, J., Ly, H. & Liang, Y. (2015). *Journal of Virology*. **89**, 2944–2955.
- Yekwa, E., Aphibanthammakit, C., Carnec, X., Coutard, B., Picard, C., Canard, B., Baize, S. & Ferron, F. (2019). *Arenaviridae* exoribonuclease presents genomic RNA edition capacity BioRxiv.
- Yekwa, E., Khourieh, J., Canard, B., Papageorgiou, N. & Ferron, F. (2017). *Acta Crystallographica Section D Structural Biology*. **73**, 641–649.
- Yun, N. E., Ronca, S., Tamura, A., Koma, T., Seregin, A. V., Dineley, K. T., Miller, M., Cook, R., Shimizu, N., Walker, A. G., Smith, J. N., Fair, J. N., Wauquier, N., Bockarie, B., Khan, S. H., Makishima, T. & Paessler, S. (2015). *Journal of Virology*. **90**, 2920–2927.
- Yun, N. E. & Walker, D. H. (2012). *Viruses*. **4**, 2031–2048.

Zahn, K. E., Tchesnokov, E. P., Götte, M. & Doublié, S. (2011). *The Journal of Biological Chemistry*. **286**, 25246–25255.

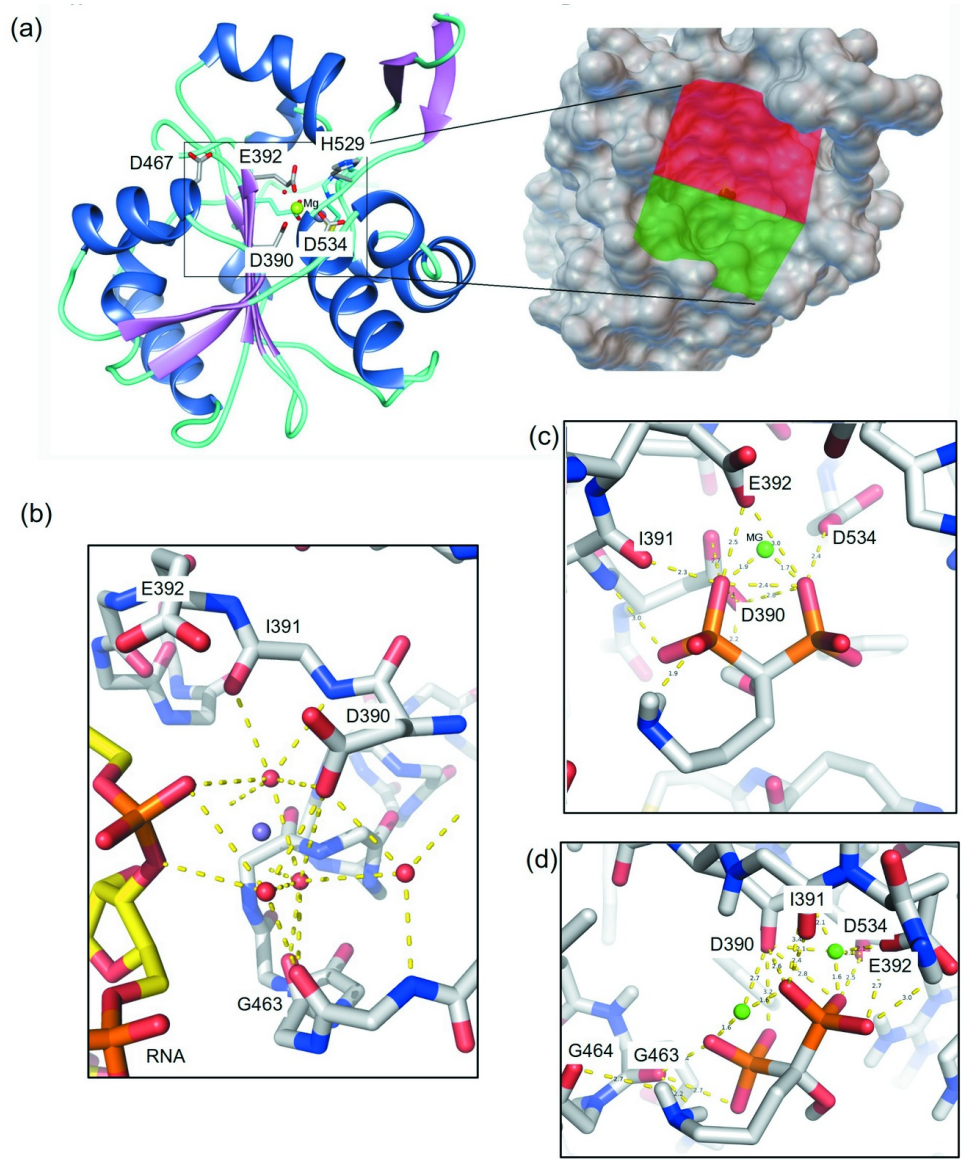


Figure 1

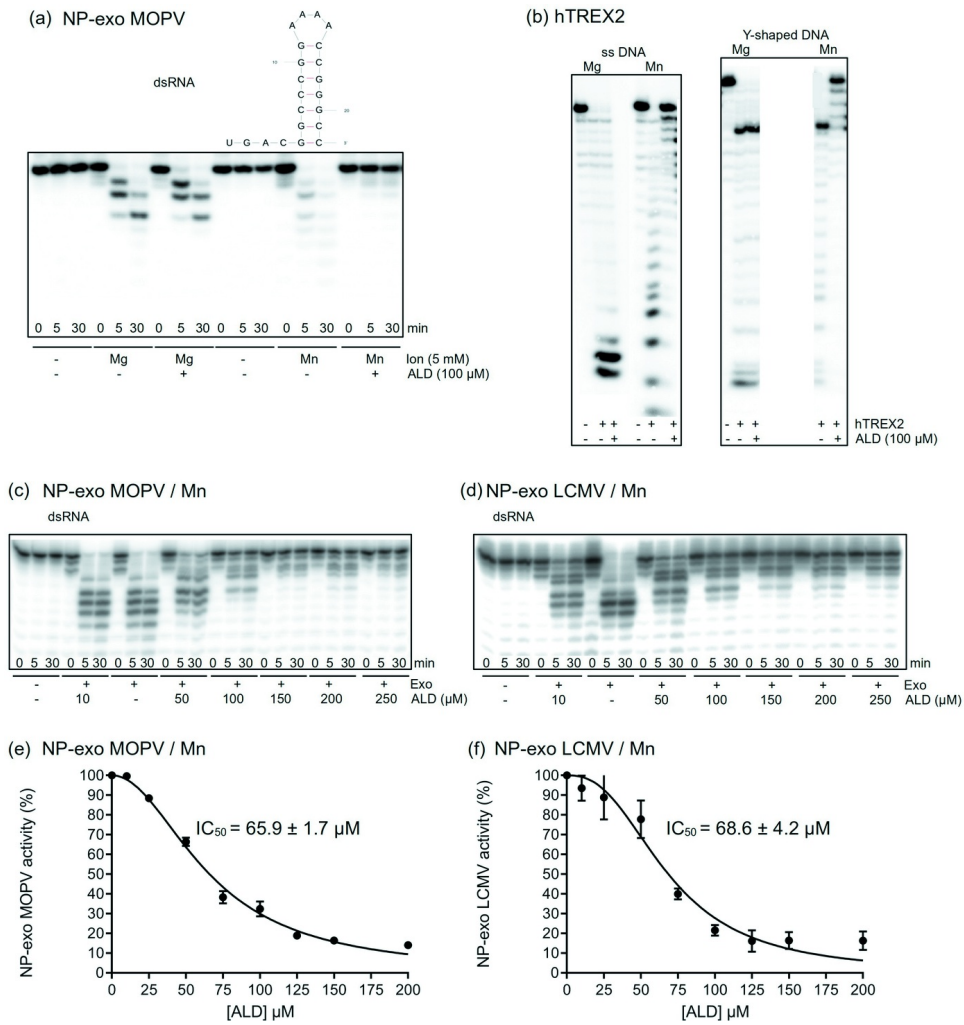


Figure 2

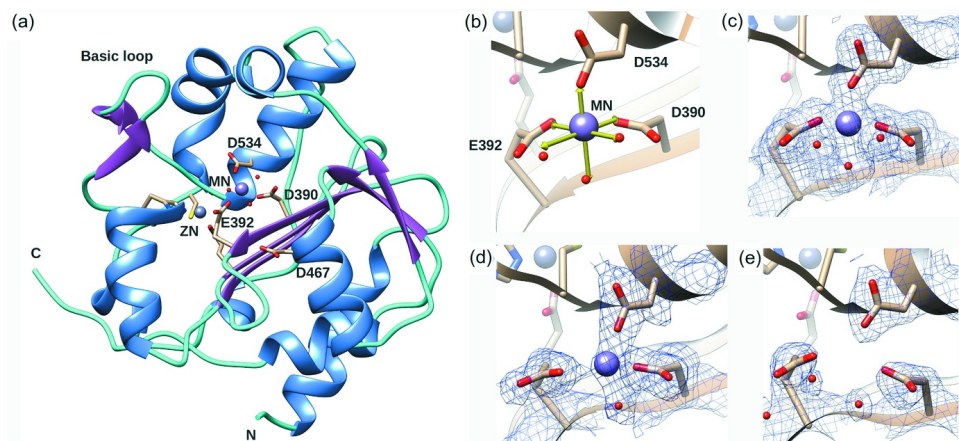


Figure 3

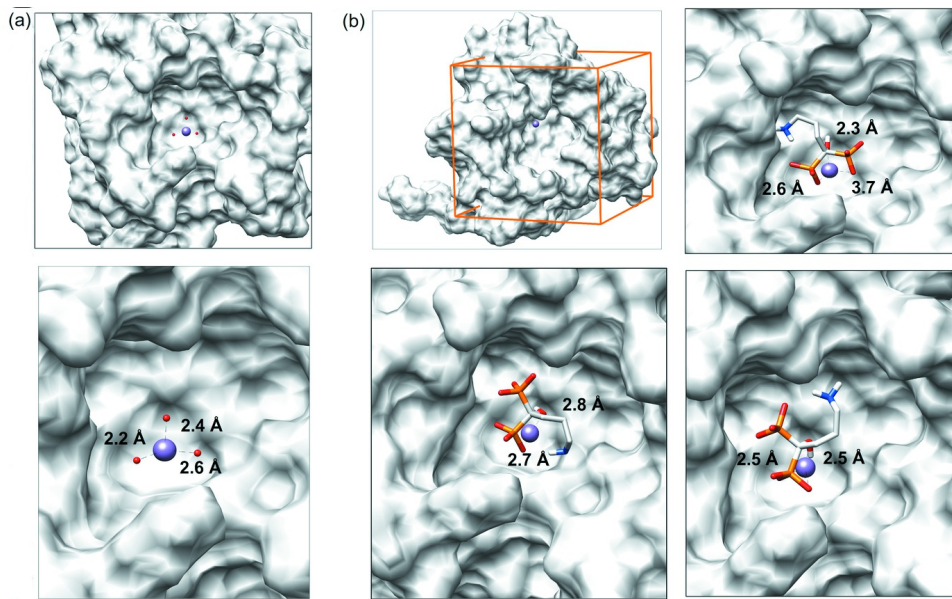
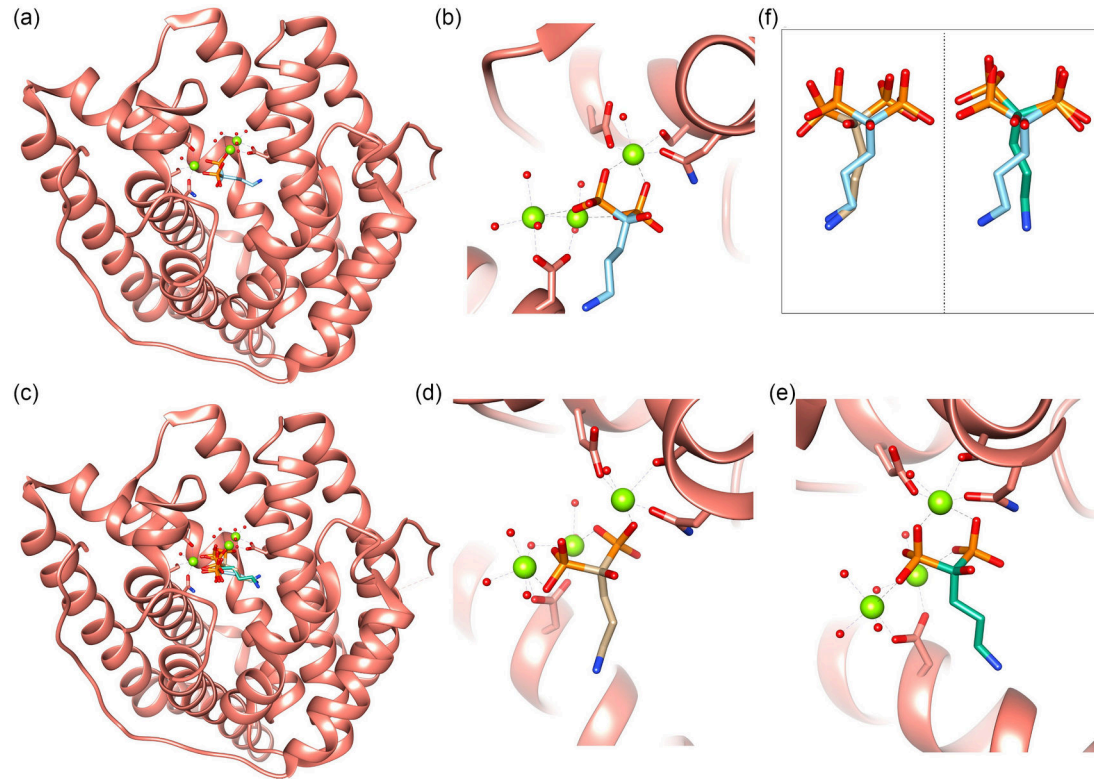


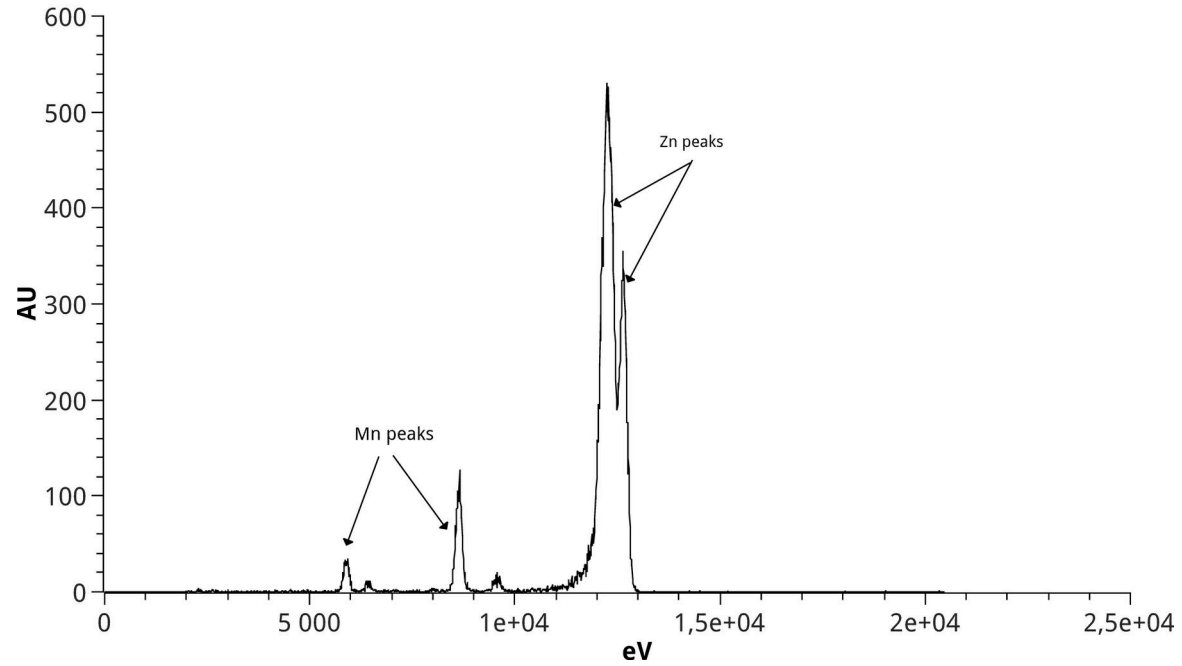
Figure 4

SF1



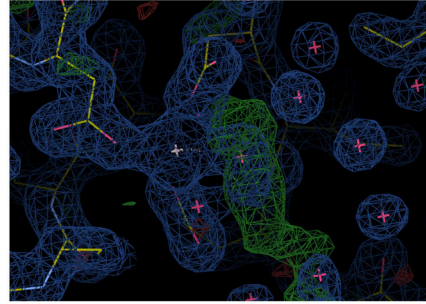
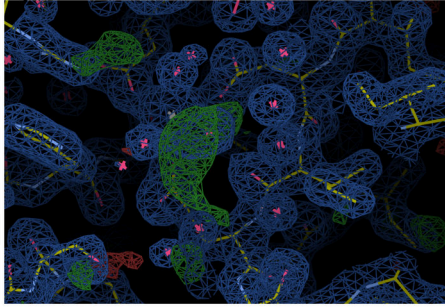
SF2

XRF ion characterization



SF3

(a)



(b)

